

# Finite Element Model-based Tumor Registration of microPET and High-resolution MR Images for Photodynamic Therapy in Mice

Baowei Fei <sup>a,b,\*</sup>, Hesheng Wang <sup>b</sup>, Raymond F. Muzic Jr. <sup>a,b</sup>, Chris A. Flask <sup>a</sup>,  
Denise K. Feyes <sup>c</sup>, David L. Wilson <sup>b,a</sup>, Jeffrey L. Duerk <sup>a,b</sup>, Nancy L. Oleinick <sup>c</sup>

<sup>a</sup> Department of Radiology, Case Western Reserve University and  
University Hospitals of Cleveland, 11100 Euclid Avenue, OH 44106

<sup>b</sup> Department of Biomedical Engineering, Case Western Reserve University, OH 44106

<sup>c</sup> Department of Radiation Oncology, Case Western Reserve University, OH 44106

## ABSTRACT

We are investigating imaging techniques to study the tumor response to photodynamic therapy (PDT). PET can provide physiological and functional information. High-resolution MRI can provide anatomical and morphological changes. Image registration can combine MRI and PET images for improved tumor monitoring. In this study, we acquired high-resolution MRI and microPET [<sup>18</sup>F]fluorodeoxyglucose (FDG) images from C3H mice with RIF-1 tumors that were treated with Pc 4-based PDT. For tumor registration, we developed a finite element model (FEM)-based deformable registration scheme. To assess the registration quality, we performed slice by slice review of both image volumes, computed the volume overlap ratios, and visualized both volumes in color overlay. The mean volume overlap ratios for tumors were 94.7% after registration. Registration of high-resolution MRI and microPET images combines anatomical and functional information of the tumors and provides a useful tool for evaluating photodynamic therapy.

Keywords: Deformable image registration, photodynamic therapy, finite element model, small animal imaging, cellular and molecular imaging, and cancer.

## 1. INTRODUCTION

Photodynamic therapy (PDT) is a relatively new therapeutic modality for cancer treatment.<sup>1</sup> With PDT, a tumor-localized photosensitizer is irradiated with visible light to generate reactive oxygen that efficiently kills cells and ablates tumors.<sup>1</sup> PDT can be administered deep into tumors using minimally invasive techniques as only the small laser fiber that delivers the light to the tumor needs to be inserted into the lesions. PDT with Photofrin is US-FDA approved for treating early and advanced lung cancer, advanced esophageal cancer, and Barrett's esophagus.<sup>1</sup> An important advantage of PDT is that both the photosensitizer and the light are inert by themselves, and the light can be precisely focused onto a selected region, allowing extreme specificity in the localization of the photodynamic effect. Consequently, systemic toxicities are minimized.

---

\* E-mail: Baowei.Fei@case.edu, Phone: 216-844-5281, Department of Radiology, Case Western Reserve University and University Hospitals of Cleveland, 11100 Euclid Avenue, Cleveland, OH 44106-5056.

Imaging techniques provide a useful tool for assessing PDT efficacy. First, magnetic resonance imaging (MRI) has been used to evaluate PDT-induced vascular damage followed by hemorrhagic necrosis in murine M1 tumors in mice.<sup>2</sup> Blood oxygenation level-dependent (BOLD) contrast MRI shows attenuation (25-40%) of MR signal at the treated tumor site.<sup>3</sup> Decreases in contrast agent uptake rates following PDT were observed by gadolinium contrast MRI.<sup>4</sup> Second, *in vivo* <sup>31</sup>P nuclear magnetic resonance (NMR) has been used to monitor tumor metabolic status before and after the treatment of RIF-1 tumors<sup>5,6</sup> and mammary carcinoma.<sup>7,8</sup> The NMR data revealed significant differences in the time course of high energy phosphate levels in combined hyperthermia and photodynamic therapies.<sup>7</sup> It was also demonstrated that there is a relationship between NMR measurements immediately following PDT and the ultimate effect on the tumor.<sup>6</sup> Third, diffusion-weighted MRI showed a biphasic change in the apparent diffusion coefficient (ADC) within the first 24 hours post-PDT, indicating the early response of PC-14 tumors to PDT.<sup>9</sup> Fourth, use of positron emission tomography (PET) with <sup>18</sup>F-fluorodeoxyglucose (FDG) to image mice after PDT has shown that the tumor FDG uptake decreased immediately after PDT as reported by our group<sup>10</sup> and others.<sup>11</sup>

We are combining multiple imaging modalities for monitoring PDT efficacy. For example, PET can image the rapid biochemical and physiological responses of tumors to PDT whereas MRI provides superior assessment of anatomical information, location, and morphological changes within tumors. Combining PET and MRI has several advantages. (1) MRI scans provide anatomical reference for the PET images. (2) Fusion of MRI and PET images can enhance our ability to visualize the distribution of a radio-labeled pharmaceutical. (3) MRI provides tumor shape and size information that can be used to improve the accuracy of the PET data analysis, such as drawing regions of interests (ROIs) and performing quantitative analyses. (4) MRI can be used to correct PET data for partial volume effects to clarify that the PET-measured changes induced by PDT are due to metabolic and hemodynamic changes and not to artifacts of changes in tumor size.

In this study, we focus on registration methods for MRI and PET images. Rigid-body registration algorithms for MRI and PET images have been used for human brain,<sup>12-18</sup> for the rat brain,<sup>19,20</sup> and for the cat brain.<sup>21</sup> Deformable registration is required whenever the subject is in different positions or the organ is deformed.<sup>22</sup> Finite element models (FEMs) have been used for registration of the brain,<sup>23,24</sup> the lung,<sup>25</sup> the prostate,<sup>26</sup> and coronary arteries.<sup>27</sup> These methods were applied to register images from the same modality. Thin-plate spline based registration techniques were reported by us<sup>28</sup> as well as others.<sup>29-31</sup> These methods were mainly used for human image registration. When applying the current methods to multimodality mouse registration, several challenges arise because (1) a mouse is much smaller than a human; (2) the mouse body is very flexible and thus often deforms between imaging procedures.

In the report, we describe a deformable registration method for tumor microPET and MR images. We performed imaging and PDT experiments on tumor-bearing mice. We also report the registration results from visual inspection and quantitative measurements.

## 2. MATERIALS AND METHODS

### 2.1 Animal preparation

RIF (Radiation-induced fibrosarcoma)-1 cells were grown as monolayers in E-MEM supplemented with 15% fetal bovine serum.<sup>32</sup> Prior to inoculation, C3H/HeN mice were shaved and depilated. Two tumors were initiated in each mouse by injection of  $10^5$  -  $10^6$  RIF-1 cells intradermally on the shoulder flanks.

Tumors were treated and imaged when they reached 3-5 mm in diameter, which required 7-10 days after implantation. Animals were given the photosensitizer Pc 4 (1 mg/kg) by tail vein injection. We know from experience that neither the light nor the photosensitizer alone produces any response. After 48 hours, one of the two tumors was exposed to red light (670 nm) from a diode laser (150 J/cm<sup>2</sup>; 150 mW/cm<sup>2</sup>). The other tumor in each animal served as a control (receiving photosensitizer but no light). The animals were also studied by microPET and MR imaging.

## 2.2 Image Acquisitions

Two days after photosensitizer injection, the animals were taken to the imaging facility. The mouse MR images were acquired using a Siemens Sonata 1.5 T scanner (Siemens Medical Systems, Erlangen, Germany). A dedicated custom-designed whole-body mouse coil (2-element phased-array, ID = 32 mm) was used to minimize noise levels. A T1-weighted spin echo pulse sequence (TR/TE=600/13ms) with a slice thickness of 1 mm was used to generate high-resolution coronal images (Matrix: 256 x 120, FOV: 80 x 36-mm, Pixel size: 0.3 x 0.3-mm). The acquisition time for an image slice was 72 sec. In these T1-weighted images, the tumors are clearly delineated by the bright subcutaneous fat signal. We acquired 3-5 MR image volumes from each mouse.

After MR image acquisition, the animals and the laser system were taken to the PET imaging facility. We used a microPET R4 scanner (Concorde Microsystems, Inc., Knoxville, TN 37932) designed specifically for imaging small rodents.<sup>33</sup> We followed a single animal over 90-minute period of time and monitored the response to PDT and the outcome. We used <sup>18</sup>F-FDG that is the standard radiopharmaceutical used in PET scanning for tumor diagnosis and assessment. It was produced for this experiment in standard fashion. We acquired both transmission and emission images from the same mouse. Since the animal was anesthetized and remained in the same position during the imaging session, we assume that there was no movement between the PET transmission and emission scans. One PET image volume includes 63 transverse slices covering the whole mouse and each slice has 128x128-pixel with an in-plane pixel size of 0.85 x 0.85-mm and a thickness of 1.2 mm. From each mouse, we acquired 10-22 dynamic PET image volumes. The total FDG activity for the period of 90 min was also computed to create another PET image volume. We used these volumes for registration experiments.

## 2.3 Image Processing

We used interpolation to create isotropic MR volumes before registration. The input MR volume is a 2D MR acquisition with a pixel size of 0.3x0.3-mm and a slice thickness of 1.0-mm. Twenty nine coronal slices cover the whole mouse. Using a sinc-linear interpolation, we created isotropic voxels of 0.3 mm on a side for both PET and MR image volumes. We use IDL (Interactive Data Language, Research System Inc., Boulder, CO) as the programming language.

For the purposes of deformable registration, we optionally cropped image slices that were not of interest. In the present case, because the tumors were on the mouse back near the shoulder, we cropped out images at the head and abdomen. For example, a typical image volume was 350x250x250-voxel covering the whole mouse before cropping. After cropping, we created a volume with 148x80x90-voxel near the region of interest. Cropping can bring two advantages for the tumor registration. First, cropping out regions that are not of interest can increase image consistency for the mutual information registration. Since the mouse body is very flexible, the deformation at the abdomen can cause inconsistency for the registration. Second, the small number of voxels after cropping can increase the speed of image registration.

## 2.4 Deformable Tumor Registration

At the first step, we applied the rigid-body normalized mutual information-based registration algorithm to align the cropped MRI and microPET images.<sup>34</sup> After registration, we manually segmented the tumor slice-by-slice on both high-resolution MRI and microPET image volumes.

In the second step, we developed a finite element model (FEM)-based deformable registration algorithm. For a linear elastic continuum with no initial stresses and strains, the deformation energy  $E$  of an elastic body submitted to externally applied forces can be expressed as<sup>23</sup>

$$E = \frac{1}{2} \int_{\Omega} \boldsymbol{\sigma}^T \boldsymbol{\varepsilon} d \Omega + \int_{\Omega} \mathbf{F} \cdot \mathbf{u} d \Omega$$

Where  $\mathbf{u}$  is the displacement vector,  $\Omega$  is the elastic body,  $\boldsymbol{\sigma}$  is the stress vector,  $\boldsymbol{\varepsilon}$  is the strain vector, and  $\mathbf{F}$  is the force applied to the elastic body. For a material with the maximum symmetry, *i.e.* an isotropic material, the material properties are the same in every direction. There are only two independent parameters for the stress and strain vectors ( $\boldsymbol{\sigma}$  and  $\boldsymbol{\varepsilon}$ ): the Young's modulus that relates tension and stretch, and the Poisson ratio that is the ratio of the lateral contraction due to the longitudinal stretch.

The displacement field  $\mathbf{u}$  within each element is approximated as an assembly of discrete elements interconnected at the nodal points on the element boundaries. The elements we used are tetrahedra for the volumes and triangles for the surfaces. We built the meshes for the tumor surfaces using commercial software AMIRA (Mercury Computer Systems, Inc, Chelmsford, MA). The tumor surfaces were then imported to the finite element analysis software FEMLAB (COMSOL, Inc., Burlington, MA). The tumor defined by the surface is partitioned into union of tetrahedral elements using an unstructured meshing method in FEMLAB. Over 500,000 tetrahedral solid elements were created to represent the solid tumor model. The boundary condition was defined at the surface vertices (> 800). For each surface vertex on the MRI model, we compute its distances to the surface vertices on the PET model. The closest vertex is the corresponding point. The displacement fields of the surface vertices serves as the boundary motion of the tumor. No additional external force is applied to the tumor model.

The registration approach deforms the tumor surface from the MRI volume toward that from the PET image. The displacements at the surface vertices are the force that drives the elastic surface from MRI toward that from the PET image. The tumor was modeled as a linear isotropic elastic material with Young's modulus of 60 kPa and Poisson's ratio of 0.49.<sup>35</sup> The FEM model was used to infer volumetric deformation of the tumor from the surface. The force is integrated over each element and is distributed over the nodes belonging to the element using its shape functions. After obtaining the displacement field for all vertices, we used a linear interpolation to obtain the deformed image volume of the tumor.

## 2.5. Registration Evaluation

A variety of qualitative and quantitative methods were used to evaluate the registration of microPET and high-resolution MRI. First, we used visual inspection methods to evaluate the registration quality. (1) Color overlay

displays provide a useful tool to evaluate structure overlap. We have found that rendering one image in gray and the other in red with a manually adjustable transparency scale, provides a very good way to visually determine registration accuracy.<sup>36</sup> (2) We used a checkerboard display whereby we divided the reference and registered images into sectors and created an output image by alternating sectors from the two input images.<sup>37</sup> Even small shifts of edges therefore are clearly visible. (3) We used 3D volume rendering and color overlap to visualize registration results.

Second, quantitative registration errors were computed. (1) We manually segmented the tumor boundaries in image slices and copied them to corresponding slices from other registered volumes.<sup>28</sup> From each segmented slice, we compute the center of the lesion. From the segmented boundaries across all slices, we compute the centroids of the lesion in 3-D space. This enables offline visual determination of the registration quality. By manually segmenting the lesion from multiple volumes, centroid distances and volume overlap ratios (VOR) are derived to evaluate the registration quality. The VOR is defined as the overlap volume and divided by the average of the volumes measured from MRI and PET images. A VOR value ranges from 0 (no overlap) to 1 (full overlap). (2) We measure the consistency errors for the deformable registration.<sup>38</sup> We transform a voxel in Volume A to Volume B and then transform it back to A. The distances between the corresponding voxel after the two deformable transformations serves as a measure of the registration consistent errors.

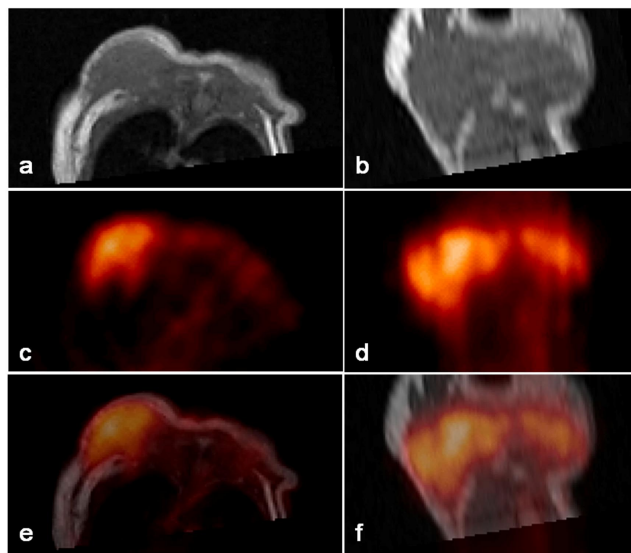


Figure 1. Registration and fusion of MRI and microPET images in transverse (left) and coronal (right) orientations. Top: MR images that cover the tumor region. Middle: Corresponding PET emission image. Bottom: Color overly of the MRI (gray) and microPET (red) images. The fusion images show that the tumors were aligned.

### 3. RESULTS AND DISCUSSION

In Figure 1, we show the results of tumor registration after rigid-body transformation. The color overlay of the MRI and microPET images demonstrates good registration of the tumor in both transverse and coronal slices indicating that the tumors are aligned in three dimensions.

To evaluate the rigid-body registration of the tumor, we manually segmented it from both MRI and microPET images and then used 3D meshes to represent the tumor surfaces. In Figure 2, the 3D visualization shows that the tumor deformed between the two imaging sessions. In order to evaluate manual segmentation errors, two observers segmented each tumor three times. The volume overlap ratios of the six segmentations are  $95.0\% \pm 1.0\%$  and  $92.0\% \pm 2.6\%$  for MRI and PET images, respectively. This indicates excellent repeatability.

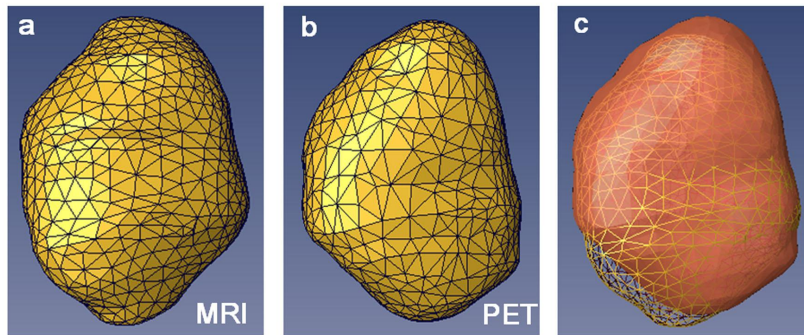


Figure 2. Meshes of a tumor. (a) Tumor segmented from a high-resolution MR volume. (b) Same tumor from the corresponding microPET emission images. (c) Color overlay of the tumor from MRI (yellow) and microPET (red). The tumor deformed during the two imaging sessions.

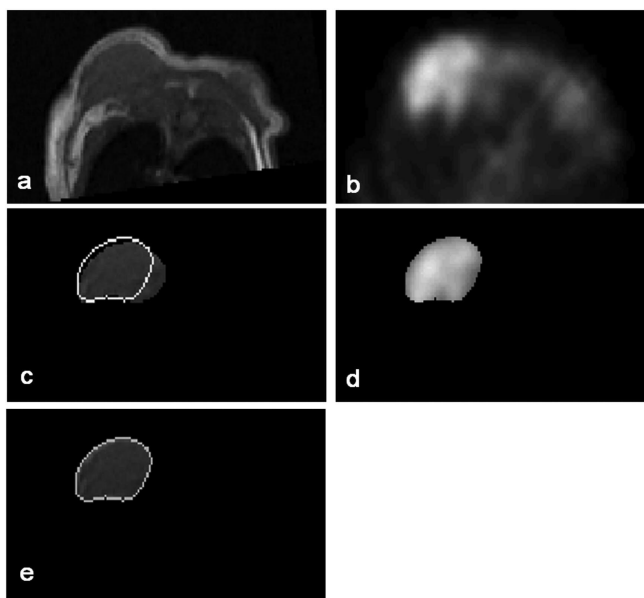


Figure 3. Comparison of rigid and deformable registration. Images on the top are the corresponding MRI (a) and microPET (b) images after rigid-body registration. The tumor on both images was manually segmented for registration evaluation (c and d). The tumor contour from the microPET image (d) is copied to the MR image (c). The contour mismatch is due to the tumor deformation. After deformable registration, the tumor on the MRI is warped and matched with that from the microPET image (e). Other slices are also matched indicating excellent tumor registration in three dimensions.

In Figure 3, we compare the results of rigid and deformable registration. The contour overlap shows that the deformable method is better than the rigid-body registration. This is consistent with quantitative measures. The NMI values increased from  $0.06 \pm 0.01$  to  $0.12 \pm 0.02$  after deformable registration. The volume overlap ratios were also improved from  $86.3\% \pm 2.5\%$  to  $94.7\% \pm 1.5\%$  with deformable registration. The mean consistency error is less than 0.1-mm for the deformable registration.

The treated tumor has less FDG uptake than the control indicating the effect of PDT. This is consistent with the microPET images (Figure 1). Fusion of PET with MRI aids in defining regions of interest on PET images for quantitative measurements. The tumor registration and fusion methods are quite useful for this application.

## 5. DISCUSSION AND CONCLUSION

The deformable registration method is quite accurate for the tumor registration. Because the tumors on both MRI and microPET images were already segmented, the registration quality was well controlled. The deformable registration performs better than the rigid-body method whenever there are deformations of the tumors. Using a Pentium IV computer (3.4 MHz CPU and 3.0 GBytes memory) and FEMLAB program, the computation time for the deformable transformation is less than four minutes.

The MR image quality was excellent because we used a dedicated mouse coil. Though a clinical 1.5 T MR scanner was used for the mouse imaging, we achieved a high in-plane pixel size of 100 x 100- $\mu$ m for small animal imaging. Future experiments will be performed on two new Bruker Biospec superconducting MR imaging systems (9.4 T and 7 T) at our institution.

Tumors respond rapidly to photodynamic therapy, and there is great potential for studying in vivo responses with PET and with MRI either during the photoirradiation or within a short time thereafter. It will be important to ensure that changes in metabolic parameters, as measured by PET imaging, are properly assigned to the treated tumor or other tissue of interest. Deformable image registration should improve the ability to quantitatively evaluate the desired responses.

In conclusion, we have developed a deformable registration method for tumor MRI and microPET images. The image registration and fusion provided both functional and anatomic information for evaluating photodynamic therapy in mice. This method could provide a powerful tool for other applications of small animal imaging in cancer biology, functional genomics, and drug development.

#### ACKNOWLEDGEMENTS

The algorithm developed in this research was supported by the DOD Award DAMD17-02-1-0230 and the Case Comprehensive Cancer Center Pilot Award to Baowei Fei.

#### Reference List

- 1 T.J.Dougherty, "An update on photodynamic therapy applications," *J Clin.Laser Med Surg.*, vol. 20, pp. 3-7, Feb, 2002.
- 2 B.G.Winsborrow, H.Grondey, H.Savoie, C.A.Fyfe, and D.Dolphin, "Magnetic resonance imaging evaluation of photodynamic therapy-induced hemorrhagic necrosis in the murine M1 tumor model," *Photochem.Photobiol.*, vol. 66, pp. 847-852, Dec, 1997.
- 3 S.Gross, A.Gilead, A.Scherz, M.Neeman, and Y.Salomon, "Monitoring photodynamic therapy of solid tumors online by BOLD-contrast MRI," *Nat.Med.*, vol. 9, pp. 1327-1331, Oct, 2003.
- 4 S.D.Kennedy, L.S.Szczepaniak, S.L.Gibson, R.Hilf, T.H.Foster, and R.G.Bryant, "Quantitative MRI of Gd-DTPA uptake in tumors: response to photodynamic therapy," *Magn Reson Med*, vol. 31, pp. 292-301, Mar, 1994.
- 5 J.Mattiello, J.L.Evelhoch, E.Brown, A.P.Schaap, and F.W.Hetzel, "Effect of photodynamic therapy on RIF-1 tumor metabolism and blood flow examined by  $^{31}\text{P}$  and  $^2\text{H}$  NMR spectroscopy," *NMR Biomed*, vol. 3, pp. 64-70, Apr, 1990.
- 6 J.C.Bremner, S.R.Wood, J.K.Bradley, J.Griffiths, G.E.Adams, and S.B.Brown, " $^{31}\text{P}$  magnetic resonance spectroscopy as a predictor of efficacy in photodynamic therapy using differently charged zinc phthalocyanines," *Br.J Cancer*, vol. 81, pp. 616-621, Oct, 1999.
- 7 Q.Jiang, M.Chopp, and F.W.Hetzel, "In vivo  $^{31}\text{P}$  NMR study of combined hyperthermia and photodynamic therapies of mammary carcinoma in the mouse," *Photochem.Photobiol.*, vol. 54, pp. 795-799, Nov, 1991.
- 8 Y.H.Liu, R.M.Hawk, and S.Ramaprasad, "In vivo relaxation time measurements on a murine tumor model--prolongation of T1 after photodynamic therapy," *Magn Reson Imaging*, vol. 13, pp. 251-258, 1995.
- 9 V.Plaks, N.Koudinova, U.Nevo, J.H.Pinthus, H.Kanety, Z.Eshhar, J.Ramon, A.Scherz, M.Neeman, and Y.Salomon, "Photodynamic therapy of established prostatic adenocarcinoma with TOOKAD: a biphasic apparent diffusion coefficient change as potential early MRI response marker," *Neoplasia.*, vol. 6, pp. 224-233, May, 2004.

- 10 B.W.Fei, R.Muzic, Z.Lee, C.Flask, R.Morris, J.L.Duerk, and D.L.Wilson, "Registration of micro-PET and high resolution MR images of mice for monitoring photodynamic therapy," *Proceeding of SPIE on Medical Imaging: Physiology, Function, and Structure from Medical Images*, pp. 371-379, 2004.
- 11 D.Lapointe, N.Brasseur, J.Cadorette, C.La Madeleine, S.Rodrigue, J.E.van Lier, and R.Lecomte, "High-resolution PET imaging for in vivo monitoring of tumor response after photodynamic therapy in mice," *J Nucl.Med*, vol. 40, pp. 876-882, May, 1999.
- 12 J.Cizek, K.Herholz, S.Vollmar, R.Schrader, J.Klein, and W.D.Heiss, "Fast and robust registration of PET and MR images of human brain," *Neuroimage.*, vol. 22, pp. 434-442, May, 2004.
- 13 R.Myers, "The application of PET-MR image registration in the brain," *Br.J Radiol*, vol. 75 Spec No, pp. S31-S35Nov, 2002.
- 14 W.M.Wells, III, P.Viola, H.Atsumi, S.Nakajima, and R.Kikinis, "Multi-modal volume registration by maximization of mutual information," *Med.Image Anal.*, vol. 1, pp. 35-51, Mar, 1996.
- 15 J.C.Wong, C.Studholme, D.J.Hawkes, and M.N.Maisey, "Evaluation of the limits of visual detection of image misregistration in a brain fluorine-18 fluorodeoxyglucose PET-MRI study," *Eur.J.Nucl.Med.*, vol. 24, pp. 642-650, Jun, 1997.
- 16 C.Studholme, D.L.Hill, and D.J.Hawkes, "Automated three-dimensional registration of magnetic resonance and positron emission tomography brain images by multiresolution optimization of voxel similarity measures," *Med Phys.*, vol. 24, pp. 25-35, Jan, 1997.
- 17 L.Thurfjell, Y.H.Lau, J.L.Andersson, and B.F.Hutton, "Improved efficiency for MRI-SPET registration based on mutual information," *Eur.J Nucl Med*, vol. 27, pp. 847-856, Jul, 2000.
- 18 S.J.Kiebel, J.Ashburner, J.B.Poline, and K.J.Friston, "MRI and PET coregistration--a cross validation of statistical parametric mapping and automated image registration," *Neuroimage.*, vol. 5, pp. 271-279, May, 1997.
- 19 N.Hayakawa, K.Uemura, K.Ishiwata, Y.Shimada, N.Ogi, T.Nagaoka, H.Toyama, K.Oda, A.Tanaka, K.Endo, and M.Senda, "A PET-MRI registration technique for PET studies of the rat brain," *Nucl.Med Biol.*, vol. 27, pp. 121-125, Feb, 2000.
- 20 D.J.Rubins, W.P.Melega, G.Lacan, B.Way, A.Plenevaux, A.Luxen, and S.R.Cherry, "Development and evaluation of an automated atlas-based image analysis method for microPET studies of the rat brain," *Neuroimage.*, vol. 20, pp. 2100-2118, Dec, 2003.
- 21 Y.Shimada, K.Uemura, B.A.Ardekani, T.Nagaoka, K.Ishiwata, H.Toyama, K.Ono, and M.Senda, "Application of PET-MRI registration techniques to cat brain imaging," *J Neurosci.Methods*, vol. 101, pp. 1-7, Aug 15, 2000.
- 22 W.R.Crum, T.Hartkens, and D.L.Hill, "Non-rigid image registration: theory and practice," *Br.J.Radiol.*, vol. 77 Spec No 2, pp. S140-S1532004.
- 23 M.Ferrant, A.Nabavi, B.Macq, F.A.Jolesz, R.Kikinis, and S.K.Warfield, "Registration of 3-D intraoperative MR images of the brain using a finite-element biomechanical model," *Ieee Transactions on Medical Imaging*, vol. 20, pp. 1384-1397, 2001.
- 24 M.I.Miga, K.D.Paulsen, P.J.Hoopes, F.E.Kennedy, Jr., A.Hartov, and D.W.Roberts, "In vivo quantification of a homogeneous brain deformation model for updating preoperative images during surgery," *IEEE Trans.Biomed.Eng*, vol. 47, pp. 266-273, Feb, 2000.
- 25 T.Zhang, N.P.Orton, T.R.Mackie, and B.R.Paliwal, "Technical note: A novel boundary condition using contact elements for finite element based deformable image registration," *Med.Phys.*, vol. 31, pp. 2412-2415, Sep, 2004.
- 26 A.Bharatha, M.Hirose, N.Hata, S.K.Warfield, M.Ferrant, and K.H.Zou, "Three-dimensional finite element-based deformable registration of pre- and intraoperative prostate imaging," *Radiology*, vol. 221, pp. 2242001.
- 27 A.I.Veress, J.A.Weiss, G.T.Gullberg, D.G.Vince, and R.D.Rabbitt, "Strain measurement in coronary arteries using intravascular ultrasound and deformable images," *J.Biomech.Eng*, vol. 124, pp. 734-741, Dec, 2002.
- 28 B.W.Fei, C.Kemper, and D.L.Wilson, "A comparative study of warping and rigid body registration for the prostate and pelvic MR volumes," *Computerized Medical Imaging and Graphics*, vol. 27, pp. 267-281, 2003.
- 29 J.Lian, L.Xing, S.Hunjan, C.Dumoulin, J.Levin, A.Lo, R.Watkins, K.Rohling, R.Giaquinto, D.Kim, D.Spielman, and B.Daniel, "Mapping of the prostate in endorectal coil-based MRI/MRSI and CT: a deformable registration and validation study," *Med.Phys.*, vol. 31, pp. 3087-3094, Nov, 2004.
- 30 H.Wang, L.Dong, M.F.Lii, A.L.Lee, R.de Crevoisier, R.Mohan, J.D.Cox, D.A.Kuban, and R.Cheung, "Implementation and validation of a three-dimensional deformable registration algorithm for targeted prostate cancer radiotherapy," *Int.J.Radiat.Oncol.Biol.Phys.*, vol. 61, pp. 725-735, Mar 1, 2005.

- 31 C.R.Meyer, J.L.Boes, B.Kim, P.H.Bland, K.R.Zasadny, P.V.Kison, K.Koral, K.A.Frey, and R.L.Wahl, "Demonstration of accuracy and clinical versatility of mutual information for automatic multimodality image fusion using affine and thin-plate spline warped geometric deformations," *Med Image Anal.*, vol. 1, pp. 195-206, Apr, 1997.
- 32 S.I.Zaidi, N.L.Oleinick, M.T.Zaim, and H.Mukhtar, "Apoptosis during photodynamic therapy-induced ablation of RIF-1 tumors in C3H mice: electron microscopic, histopathologic and biochemical evidence," *Photochem.Photobiol.*, vol. 58, pp. 771-776, Dec, 1993.
- 33 C.Knoess, S.Siegel, A.Smith, D.Newport, N.Richerzhagen, A.Winkeler, A.Jacobs, R.N.Goble, R.Graf, K.Wienhard, and W.D.Heiss, "Performance evaluation of the microPET R4 PET scanner for rodents," *Eur.J Nucl.Med Mol.Imaging*, vol. 30, pp. 737-747, May, 2003.
- 34 B.W.Fei, A.Wheaton, Z.Lee, J.L.Duerk, and D.L.Wilson, "Automatic MR volume registration and its evaluation for the pelvis and prostate," *Physics in Medicine and Biology*, vol. 47, pp. 823-838, 2002.
- 35 T.A.Krouskop, T.M.Wheeler, F.Kallel, B.S.Garra, and T.Hall, "Elastic moduli of breast and prostate tissues under compression," *Ultrasound.Imaging*, vol. 20, pp. 260-274, Oct, 1998.
- 36 B.W.Fei, Z.Lee, J.L.Duerk, Lewin J.S., D.B.Sodee, and D.L.Wilson, "Registration and Fusion of SPECT, High Resolution MRI, and interventional MRI for Thermal Ablation of the Prostate Cancer," *Ieee Transactions on Nuclear Science*, vol. 51, pp. 177-183, 2004.
- 37 B.W.Fei, J.L.Duerk, and D.L.Wilson, "Automatic 3D Registration for Interventional MRI-Guided Treatment of Prostate Cancer," *Computer Aided Surgery*, vol. 7, pp. 257-267, 2002.
- 38 J.He and G.E.Christensen, "Large deformation inverse consistent elastic image registration," *Inf.Process Med.Imaging*, vol. 18, pp. 438-449, Jul, 2003.

Baowei Fei, Hesheng Wang, Raymond F. Muzic, Jr., Chris A. Flask, Denise Feyes, David L. Wilson, Jeffrey L. Duerk, and Nancy L. Oleinick, "Finite element model-based tumor registration of microPET and high-resolution MR images for photodynamic therapy in mice", Armando Manduca, Amir A. Amini, Proc. SPIE 6143, 61433I (2006)

Copyright 2006 Society of Photo-Optical Instrumentation Engineers (SPIE). One print or electronic copy may be made for personal use only. Systematic reproduction and distribution, duplication of any material in this paper for a fee or for commercial purposes, or modification of the content of the paper are prohibited.

<http://dx.doi.org/10.1117/12.649531>